

High sustained average power cw and ultrafast Yb:YAG near-diffraction-limited cryogenic solid-state laser

David C. Brown*, Joseph M. Singley, Katie Kowalewski, James Guelzow, and Victoria Vitali

Snake Creek Lasers, LLC, Hallstead, Pennsylvania 18822, USA
*dbrown@snakecreeklasers.com

Abstract: We report what we believe to be record performance for a high average power Yb:YAG cryogenic laser system with sustained output power. In a CW oscillator-single-pass amplifier configuration, 963 W of output power was measured. In a second configuration, a two amplifier Yb:YAG cryogenic system was driven with a fiber laser picosecond ultrafast oscillator at a 50 MHz repetition rate, double-passed through the first amplifier and single-passed through the second, resulting in 758 W of average power output. Pulses exiting the system have a FWHM pulsewidth of 12.4 ps, an energy/pulse of 15.2 μ J, and a peak power of 1.23 MW. Both systems are force convection-cooled with liquid nitrogen and have been demonstrated to run reliably over long time periods.

© 2010 Optical Society of America

OCIS codes: (140.3460) Lasers; (140.0140) Lasers and laser optics; (140.3580) Lasers, solid state; (140.3615) Lasers, ytterbium.

References and links

1. D. C. Brown, "Ultra-high-average-power diode-pumped Nd:YAG and Yb:YAG lasers," *IEEE J. Quantum Electron.* **33**, 861–873 (1997).
2. D. C. Brown, "Nonlinear thermal and stress effects and scaling behavior of YAG slab amplifiers," *IEEE J. Quantum Electron.* **34**, 2393–2402 (1998).
3. D. C. Brown, "Nonlinear thermal distortion in YAG rod amplifiers," *IEEE J. Quantum Electron.* **34**, 2383–2392 (1998).
4. T. Y. Fan, T. Crow, and B. Hoden, "Cooled Yb:YAG for high-power solid-state lasers," *Proc. SPIE* **3381**, 200–205 (1998) (Note: A Reviewer of this paper has indicated that operation of Yb:YAG at cryogenic temperatures was achieved prior to this reference, but provided no details. We have been unable to confirm this based on our search of the open literature.).
5. P. A. Schulz, and S. R. Henion, "Liquid-nitrogen-cooled Ti:Al₂O₃ laser," *IEEE J. Quantum Electron.* **27**, 1039–1047 (1991).
6. G. Erbert, I. Bass, R. Hackel, S. Jenkins, K. Kanz, and J. Paisner, "43-w, CW Ti:sapphire laser," in *Conference on Lasers and Electro-Optics*, vol. 10 of 1991 Technical Digest Series (Optical Society of America, Washington, DC, 1991), pp. 390–392.
7. D. C. Brown, "The promise of cryogenic solid-state lasers," *IEEE J. Sel. Top. Quantum Electron.* **11**, 587–599 (2005).
8. T. Y. Fan, D. J. Ripin, and R. L. Aggarwal, "Cryogenic Yb³⁺-doped solid-state lasers," *IEEE J. Sel. Top. Quantum Electron.* **13**, 448–459 (2007).
9. J. K. Brasseur, A. K. Abeeluck, A. R. Awtry, L. S. Meng, K. E. Shortoff, N. J. Miller, R. K. Hampton, M. H. Cuchiara, and D. K. Newmann, "2.3-kw continuous operation cryogenic Yb:YAG laser," *Proc. SPIE* **6952**, 69520L (2008).
10. S. Tokita, J. Kawanaka, Y. Izawa, M. Fujita, and T. Kawashima, "23.7-W picosecond cryogenic-Yb:YAG multipass amplifier," *Opt. Express* **15**(7), 3955–3961 (2007).
11. Y. Ahahane, M. Aoyama, K. Ogawa, K. Tsuji, S. Tokita, J. Kawanaka, H. Nishioka, and K. Yamakawa, "High-energy, diode-pumped, picosecond Yb:YAG chirped-pulse regenerative amplifier for pumping optical parametric chirped-pulse amplification," *Opt. Lett.* **31**, 1899–1901 (2007).
12. K. H. Hong, A. Siddiqui, J. Moses, J. Gopinath, J. Hybl, F. O. Ilday, T. Y. Fan, and F. X. Kärtner, "Generation of 287 W, 5.5 ps pulses at 78 MHz repetition rate from a cryogenically cooled Yb:YAG amplifier seeded by a fiber chirped-pulse amplification system," *Opt. Lett.* **33**(21), 2473–2475 (2008).

13. K. H. Hong, C. J. Lai, A. Siddiqui, and F. X. Kärtner, "130-W picosecond green laser based on a frequency-doubled hybrid cryogenic Yb:YAG amplifier," *Opt. Express* **17**(19), 16911–16919 (2009).
14. K. H. Hong, J. T. Gopinath, D. Rand, A. M. Siddiqui, S. W. Huang, E. Li, B. J. Eggleton, J. D. Hybl, T. Y. Fan, and F. X. Kärtner, "High-energy, kHz-repetition-rate, ps cryogenic Yb:YAG chirped-pulse amplifier," *Opt. Lett.* **35**(11), 1752–1754 (2010).
15. J. Dong, and M. Bass, "Dependence of the Yb³⁺ emission cross-section and lifetime on temperature and concentration in yttrium aluminum garnet," *J. Opt. Soc. Am. B* **20**, 1975–1979 (2003).
16. R. L. Aggarwal, D. J. Ripin, J. R. Ochoa, and T. Y. Fan, "Measurement of thermo-optic properties of Y₃Al₅O₁₂, Lu₃Al₅O₁₂, YAlO₃, LiYF₄, LiLuF₄, BaY₂F₈, KGd(WO₄)₂, and KY(WO₄)₂ laser crystals in the 80-300 K temperature range," *J. Appl. Phys.* **98**, 103514 (2005).
17. D. C. Brown, "High-Power Cryogenic Yb:YAG Solid-State Lasers," 6th Annual Directed Energy Symposium Proceedings, Albuquerque, NM (2003).
18. S. Tokita, J. Kawanaka, M. Fujita, T. Kawashima, and Y. Izawa, "Sapphire-conductive end-cooling of high power cryogenic Yb:YAG lasers," *Appl. Phys. B* **80**, 635–638 (2005).
19. D. C. Brown, J. M. Singley, E. Yager, J. W. Kuper, B. J. Lotito, and L. L. Bennett, "Innovative high-power CW Yb:YAG cryogenic laser," *Proc. SPIE* **6552**, 65520D (2007).
20. D. C. Brown, J. M. Singley, E. Yager, K. Kowalewski, J. Guelzow, and J. W. Kuper, "Kilowatt class high-power CW Yb:YAG cryogenic laser," *Proc. SPIE* **6952**, 69520K (2008).
21. P. Lacovara, "Energy transfer and up-conversion in Yb:YAG and Yb:Er:YAG," Ph.D. Thesis, Boston University (1992), Available from University Microfilms Inc., Ann Arbor, MI, USA.
22. Y. S. Touloukian, R. K. Kirby, R. E. Taylor, and T. Y. R. Lee, *Thermophysical Properties of Matter*, (New York: Plenum, 1977) vol. **13**
23. D. C. Brown, R. L. Cone, Y. Sun, and R. W. Equal, "Yb:YAG Absorption at ambient and cryogenic temperatures," *IEEE J. Sel. Top. Quantum Electron.* **11**, 604–612 (2005).
24. D. C. Brown, and V. Vitali, "Yb:YAG Kinetics model including saturation and power conservation," *IEEE J. Quantum Electron.* (to be published).
25. D. C. Brown, T. M. Bruno, and V. Vitali, "Saturated absorption effects in CW-pumped solid-state lasers," *IEEE J. Quantum Electron.* (to be published).
26. J. Kawanaka, "New Concept of DPSSL," US-Japan Workshop on Laser-IFE, General Atomics, San Diego (2005), <http://aries.ucsd.edu/LIB/MEETINGS/0503-USJ-LIFE/>

I. Introduction

Significant advances in cryogenically-cooled Yb:YAG lasers have made in the past decade. The use of cryogenic cooling to enhance the power scalability, and significantly reduce, or render thermally induced phase aberrations, stresses, and birefringence insignificant, in solid-state lasers was first examined in detail in [1–3]. Reference [4] describes the first experimental description of reduced thermal aberrations in cryogenically-cooled Yb:YAG lasers. Since that time, other investigators have provided further evidence of reduced thermal aberrations in Yb:YAG and Nd:YAG. Reduced thermal aberrations in Ti:Al₂O₃ lasers at cryogenic temperatures have been described in the literature as well [5,6]. References [7] and [8] provide good summaries of recent work, however, we mention some recent papers that are relevant to the results presented here. In [9] the authors describe a 2.3 kW cryogenic Yb:YAG oscillator-amplifier system whose output is quasi-CW. Here we describe a Yb:YAG cryogenic oscillator-amplifier system with sustained cw or ultrafast average power output. References [10–14] describe very recent work that use Yb:YAG cryogenic amplifiers to produce picosecond pulses at high average power at the fundamental and second harmonic wavelengths. In this paper we describe a simple direct-amplification picosecond system that avoids the use of chirped-pulse-amplification.

In addition to the substantial materials properties benefits, cryogenic cooling can also lead to favorable changes in laser properties. For Yb:YAG lasers, for example, the quasi-three-level nature of Yb at room temperature becomes almost purely four-level at 77 K (the temperature of liquid nitrogen at 1 atmosphere), eliminating ground state absorption. The stimulated-emission cross-section of Yb:YAG increases by almost a factor of five at 77 K [8,15], while the saturation intensity is reduced likewise. Yb:YAG is an almost ideal laser system at 77 K, and displays no up-conversion, concentration-quenching, or other deleterious energy transfer mechanisms.

1.1 Yb:YAG Thermal and thermo-optic properties at reduced temperatures

The predictions of significantly reduced thermal aberrations, stress, and birefringence in YAG originally presented in [1–3] were based on thermal, mechanical, and thermo-optic measurements harvested from the literature available at that time. Since then, considerably better values of the thermal conductivity, thermal expansion coefficient, and thermo-optic coefficient (dn/dT) have however been generated and published [16] for a number of solid-state laser materials. Because the thermal conductivity values presented in [16] for Yb:YAG have been used for the thermal simulations reported in this article, we summarize the data and fits to the data here. In Fig. 1, we show the thermal conductivity of Yb:YAG as a function of temperature from 100 to 300 K. The data are presented for Yb dopings of 0, 2, 4, 10, 15, and 25 at-%.

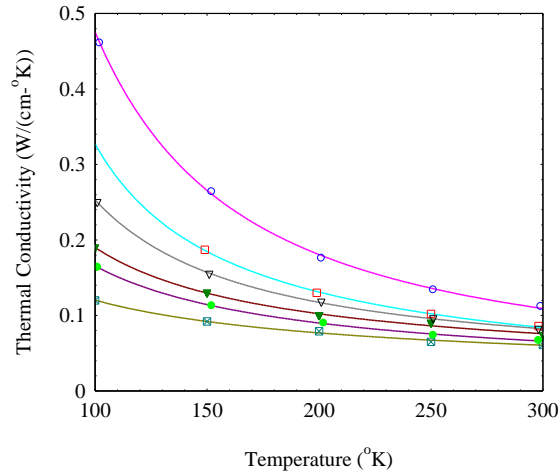


Fig. 1. Thermal conductivity of Yb:YAG as a function of absolute temperature and Yb doping density. Curves from top to bottom are 0, 2, 4, 10, 15, and 25 at-% Yb. The curves for 0, 2, 4, and 15 at-% Yb use the data of [9] while the curves for 10 and 25 at-% Yb are extrapolated from the data of [9].

It is significant that the thermal conductivity, while increasing for any doping density while temperature is reduced, is strongly dependent on the Yb doping density. This behavior has been observed for other laser materials as well [16]. For un-doped YAG the increase in thermal conductivity between 300 and 100 K is about a factor of 4.12, while for 15 at-% Yb the ratio is reduced to 2.45. Because thermal gradients in laser materials are inversely proportional to the thermal conductivity, Fig. 1 shows that despite a reduced thermal conductivity at 100 K as Yb doping increases, at any doping level meaningful reductions in thermal gradients can be obtained through cryogenic cooling. The thermal conductivity values for 0, 2, 4, and 15 at-% Yb are as reported in [16]. Values for 10 and 25 at-% Yb were generated by first fitting the data for 0, 2, 4, and 15 at-% Yb and then using the fitting functions to determine thermal conductivity as a function of doping for the fixed temperatures shown. Finally, once the thermal conductivity values were generated for 10 and 25 at-% as a function of temperature, fits were generated for 10 and 25 at-% Yb as well. The fitting function used in Fig. 1 is functionally identical to one used previously to fit YAG thermal conductivity for 0 at-% Yb doping [1], and is given by

$$k(T) = \frac{a}{(\ln(bT))^c} - \frac{d}{T}, \quad (1)$$

where a, b, c, and d are constants determined by a least-squares fit to the data. In Table 1 below, we show the values of the constants for each of the dopings shown in Fig. 1.

Table 1. Thermal Conductivity Fitting Constants For Yb:YAG

Yb Doping (at-%)	Constant a (W/(cm-K))	Constant b (1/K)	Constant c (Dimensionless)	Constant d (W/cm)
0	1.0×10^6	4.213	7.806	32.12
2	1.0×10^6	0.402	12.46	-24.20
4	1.0×10^6	8.707	7.354	52.73
10	0.7943	0.07755	2.107	-1.466
15	1.482	0.1380	2.513	-3.438
25	25.78	4.741	3.184	-4.140

For the finite-element thermal modeling we report in this paper, we have used Eq. (1) and the constants from Table 1 for 10 at-% Yb doping.

For the YAG thermal expansion coefficient α and thermo-optic coefficient $\beta = \frac{dn}{dT}$, we have used the data of [16], shown in Fig. 2. Both sets of data have been fitted using second order polynomial equations

$$\alpha(T) = (eT^2 + fT + g) \cdot 10^{-6}, \quad (2)$$

$$\beta(T) = (hT^2 + iT + j) \cdot 10^{-6}. \quad (3)$$

The values of the fitting constants e, f, g, h, i, and j are given in Table 2.

Table 2. Fitting Constants for YAG Thermal Expansion and Thermo-Optic Coefficient

e (1/(K) ³)	f (1/(K) ²)	g (1/K)	h (1/(K) ³)	i (1/(K) ²)	j (1/K)
-5.676×10^{-5}	0.04365	-1.849	-4.464×10^{-5}	0.05196	-3.793

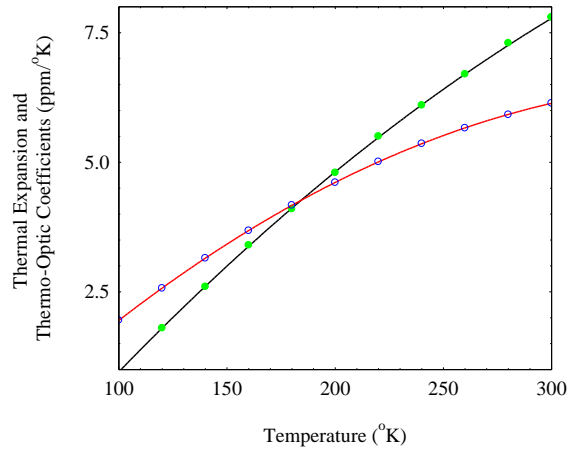


Fig. 2. Thermal expansion coefficient (●) and thermo-optic coefficient (○) as a function of temperature in the range 100-300 K for the laser material $Y_3Al_5O_{12}$.

An examination of the data displayed in Fig. 2. reveals that the thermal expansion coefficient is reduced by a factor of 3.15 when YAG is cooled from 300 to 100 K, while the thermo-optic coefficient decreases by a factor of 8.67. The increase in the thermal conductivity of YAG as temperature is lowered reduces thermal gradients (for the same input heat power density) as well as the central temperature. Phase distortions that develop as a result of the remaining thermal gradients are further reduced because of the dramatic reduction in β . Similarly, because the stresses in laser amplifiers are directly proportional to

the thermal expansion coefficient and inversely proportional to the thermal conductivity, stress and strain are much reduced as temperature is lowered and birefringence effects are minimized.

2. Design, thermal modeling, and phase distortion details

2.1 Crystal assembly

For the experiments reported in this paper, we have utilized the unique crystal assembly shown in Fig. 3. Two C-cut sapphire disks are diffusion or contact-bonded to a core Yb:YAG crystal. C-cut sapphire is used to eliminate any birefringence. Heat is rapidly removed transversely through the high thermal conductivity sapphire and is ultimately removed through indium pads to a high thermal conductivity copper heat sink assembly maintained near 77 K. This concept was first proposed and described in [17] where it was shown that at 77 K the much higher thermal conductivity of sapphire would effectively remove heat generated in the lower conductivity Yb:YAG crystal, predominantly in the direction of beam propagation, which significantly reduces thermal aberrations in the Yb:YAG crystal. At cryogenic temperatures where thermally-induced aberrations are already very small, the design shown in Fig. 3 helps to insure they remain so as average power is scaled up. This design makes possible two sided

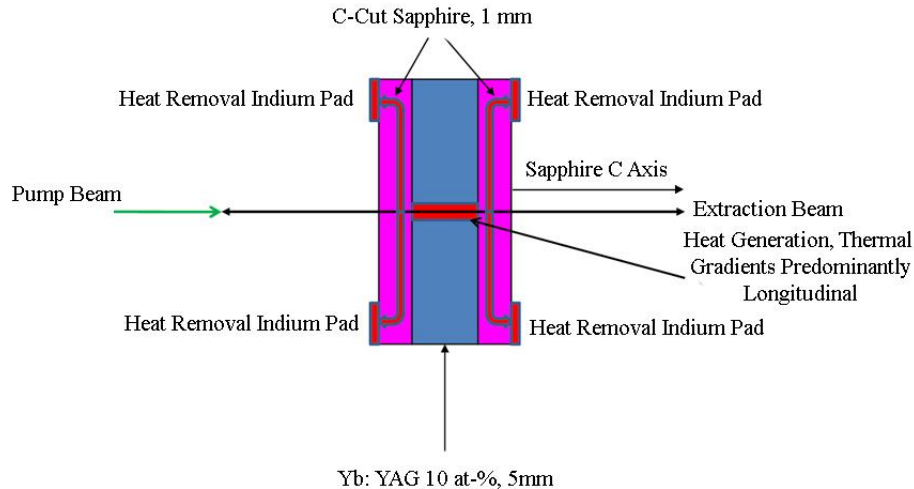


Fig. 3. Yb:YAG – Sapphire Cryogenic Crystal Assembly.

access to the Yb:YAG laser crystal so that straight-through beam extraction can occur; the symmetry of the cooling and the bonded sapphire disks assure that asymmetrical warping of the disk does not occur and that strain distortion of the Yb:YAG extraction surfaces is eliminated. The ability to symmetrically pump and cool the laser assembly, and the more flexible laser resonator designs that can be realized with straight-through extraction are decided advantages this design offers. The first experimental implementation of this crystal assembly design was reported in [18]. We have used a number of variants of this crystal assembly design and reported the operation of a 250 W near-diffraction-limited Yb:YAG cryogenic oscillator in [19], and a 550 W near-diffraction-limited Yb:YAG cryogenic oscillator in [20], using a design similar to Fig. 3, but with a 25 at-% Yb doped YAG disk with a 2 mm thickness. We have found that for a 25 at-% Yb:YAG doping, the material is unpredictable and can be contaminated with other rare earth or transition metal ions [21], resulting in less than optimal performance. For this reason we used 10 at-% material for the

experiments reported here; at that doping concentration contamination does not appear to play a significant role in performance.

The design of Fig. 3 as well as the previous design utilizing 25 at-% doped Yb:YAG work well at 77 K. With either contact-bonded or diffusion-bonded crystals, the continual cycling of the crystal assemblies between 300 and 77 K has not resulted in any de-laminations or fracture. Cooling of the crystal assemblies to 77 K typically takes about 20 minutes.

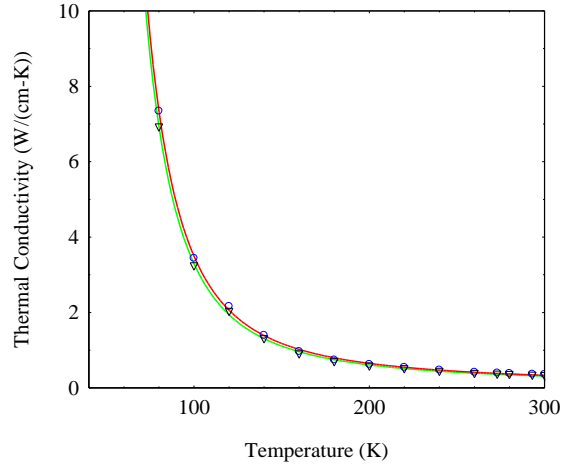


Fig. 4. Sapphire Thermal Conductivity as a Function of Temperature Perpendicular (∇) and Parallel (\circ) to the C-Axis.

For the thermal simulations to be discussed here, we show in Fig. 4. the thermal conductivity of sapphire between 300 and 60 K [22]. For this uniaxial crystal, it can be seen that the thermal conductivities parallel and perpendicular to the C-axis are nearly identical. The thermal conductivity of sapphire is large at 300 K, about 0.360 and 0.335 W/(cm-K) for the parallel and perpendicular directions, and becomes very large at 80 K, with values of 7.35 and 6.93 W/(cm-K) respectively. In contrast, the thermal conductivity of Yb:YAG with 10 at-% doping is about 0.25 W/(cm-K) at 80 K, so the ratio of the sapphire to Yb:YAG thermal conductivities is about 28.6. At temperatures near 77 K, we have found that the large thermal conductivity of sapphire results in insignificant thermal gradients in the sapphire plates enclosing the Yb:YAG crystal. The residual phase distortion through the entire crystal assembly is therefore determined almost entirely by the Yb:YAG crystal. The fitting function (Eq. (1)) previously used to model thermal conductivity as a function of temperature for Yb:YAG (Table 1) has also been used to fit the sapphire data shown in Fig. 4; the resulting fitting constants for sapphire are shown in Table 3.

Table 3. Thermal Conductivity Fitting Constants For Sapphire (Al_2O_3)

Orientation	Constant a (W/(cm-K))	Constant b (1/K)	Constant c (Dimensionless)	Constant d (W/cm)
Parallel	1.0×10^5	0.1657	10.16	-71.15
Perpendicular	9.993×10^4	0.1671	10.18	-66.18

The two Yb:YAG and sapphire crystal interfacing surfaces shown in Fig. 1. are uncoated. Nevertheless the calculated loss from the interface is very small, due to a fortuitous coincidence of the indices of sapphire (~1.76) and YAG (~1.82). The resulting Fresnel loss for normal incidence is about 0.03%. While we did not attempt to measure the actual interface loss, it is likely that it was close to the calculated value due to the small RMS surface roughness needed to diffusion-bond the two surfaces. The outside sapphire faces are dielectric coated to be anti-reflective (AR) at 1029 nm ($R < 0.01\%$), and highly transmissive (HT) at 940 nm ($R < 0.25\%$).

2.2 Diode pump sources and focusing system

As we will show in the discussion to follow, we have constructed two cryogenic pump chambers, the first (Amplifier 1) containing seven identical crystal assemblies as shown in Fig. 1, and the second pump chamber (Amplifier 2) eight crystal assemblies. Each laser disk in amplifier 1 is pumped from opposite sides using two 35 W 940 nm Limo fiber-coupled diode sources; fiber core diameter is 200 μm and the NA is 0.22. In amplifier 2, each disk is pumped with 100 W 940 nm Limo fiber coupled sources with the same core diameter and NA. The measured 940 nm output power of all diodes used to pump Amplifier 1 at 52 A current is 501.3 W. For Amplifier 2, the total measured 940 nm pump power was 1871 W. All pump diodes were cooled using closed cycle chiller systems, and the optimum wavelength match to the Yb:YAG absorption band around 940 nm obtained by varying the chiller operating temperature. The average FWHM bandwidth of all diode sources was 3.5 nm.

In order to match the diode pump beams to the resonator TEM₀₀ mode, we utilized a lens collimating and focusing system that produced a 2.0-2.1 $1/e^2$ diameter pump spot in the center of each laser crystal assembly. A 30 mm focal length collimating lens and a 250 mm focal length focusing lens were installed in a beam tube and the lens positions adjusted first for collimation and then for focusing. The average power transmission through the beam tube assembly was measured to be 96.3%. The Rayleigh range for both the 30 W and 100 W diode sources was measured to be 49.2 mm, so the pump beam is very well collimated propagating through the 5 mm thick Yb:YAG crystal.

2.3 Yb:YAG Crystal absorption modeling and measurements

In order to generate a detailed understanding of the thermal performance of the laser crystal assembly of Fig. 3, we have modeled the absorption of pump light as it propagates through the Yb:YAG crystal and the deposition of heat in the disk using a simple heat fraction model. We have used the absorption cross-sections of Yb:YAG [23] measured at 75 K to perform these calculations. Figure 5 shows the absorption cross-section of Yb:YAG as a function of wavelength. In order to determine the absorption, we have used the general Gaussian convolution equation [23]

$$A(\lambda_0, \Delta\lambda, D) = 1 - \frac{2}{\Delta\lambda} \left[\frac{\ln(2)}{\pi} \right]^{1/2} \int_{-\infty}^{\infty} (\exp(-4 \ln(2) \cdot \left[\frac{\lambda}{\lambda_0} \right]^2 \left[\frac{\lambda - \lambda_0}{\Delta\lambda} \right]^2)) \cdot \exp(-\sigma_a(\lambda) \cdot D) d\lambda. \quad (4)$$

Here, A is the absorption, λ_0 the pump diode center wavelength, $\Delta\lambda$ the full width at half maximum (FWHM) pump diode bandwidth, and D is the optical density, the ion density times the penetration depth. For the crystal assembly shown in Fig. 3, the ion density is 1.385×10^{21} ions/cm³.

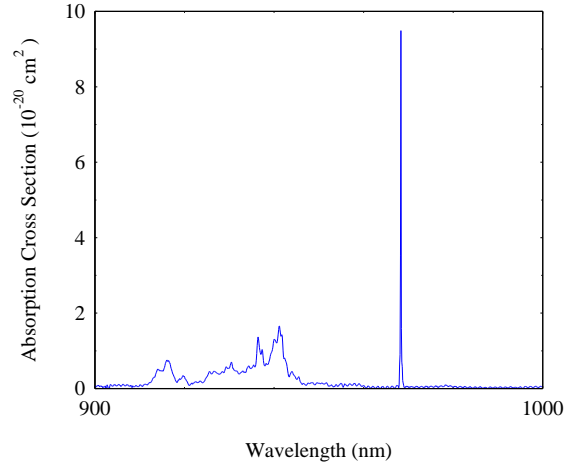


Fig. 5. Absorption cross-section of Yb:YAG as a function of wavelength at 75 K.

We have calculated the absorption as a function of penetration depth for an assumed Gaussian diode pump spectral distribution with a center wavelength of 939 nm and a FWHM bandwidth of 3 nm. The results are shown in Fig. 6. Because the absorption cannot be accurately modeled using a single exponential, we used a sum of three exponentials and performed a least-squares fit to the numerically generated absorption data. The fitting function used was of the general form

$$A(z) = 1 - (a \cdot e^{-bz} + c \cdot e^{-dz} + e \cdot e^{-fz}), \quad (5)$$

where a, b, c, d, e, and f are fitting constants, with the values shown in Table 4.

Table 4. Fitting Constants for Absorption in Yb:YAG Disk at 75 K

a	b	c	d	e	f
Dimensionless	(1/cm)	Dimensionless	(1/cm)	Dimensionless	(1/cm)
0.5195	9.611	-13.27	16.16	13.75	16.22

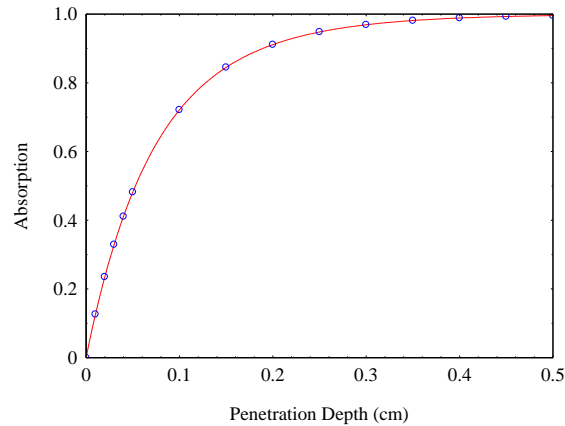


Fig. 6. Absorption of Yb:YAG at 75K as a function of penetration depth for a center wavelength of 939 nm and a FWHM bandwidth of 3 nm. Blue open circles are absorption values generated using a finite-element version of Eq. (4), and the smooth curve is a least-squares fit.

The fitting function (Eq. (5)) and the values shown in Table 4 were used in the thermal modeling results discussed in this article. The heat power density Q_h deposition in the Yb:YAG disk, a function of the radial coordinate r and longitudinal coordinate z , was modeled using the equations

$$Q_h(r, z) = -\eta_h \frac{dI_p}{dz} = \frac{2P_p \eta_h}{\pi \omega_p^2} e^{-2(\frac{r}{\omega_p})^2} (abe^{-bz} + cde^{-dz} + fge^{-gz}), \quad (6)$$

$$I_p(r, z) = I_{0p} e^{-2(\frac{r}{\omega_p})^2} \bullet T(z) = I_{0p} e^{-2(\frac{r}{\omega_p})^2} \bullet (1 - A(z)), \quad (7)$$

where η_h is the heat fraction for Yb:YAG, P_p is the incident pump power, ω_p is the pump beam waist, and the constants a , b , c , d , e , and f are the same as in Eq. (5) and Table 4. $I_p(r, z)$ is the pump intensity, a function of the radial coordinate r and longitudinal coordinate z , I_{0p} is the incident peak Gaussian intensity, and $T(z)$ and $A(z)$ are the transmission and absorption respectively. For the work reported in this paper, the heat fraction η_h was simply modeled as the quantum defect, using

$$\eta_h = 1 - \frac{\lambda_p}{\lambda_L}, \quad (8)$$

where λ_p is the pump wavelength (941 nm), and λ_L is the laser wavelength (1029 nm). It should be pointed out that we have recently found that η_h is not a constant for Gaussian beam extraction [24], but varies radially due to a radial variation in the extraction efficiency. This effect has been ignored in the modeling reported here.

As can be seen from Fig. 6, the predicted absorption at 939 nm for a 3 nm bandwidth is > 99% at a penetration depth of 5 mm, for a Yb doping of 10 at-% (5.0 at-%-cm optical thickness). Measurements of our Yb:YAG crystal assemblies have shown that as expected, for 5.0 at-%-cm optical thickness and a center wavelength of 940 nm, the absorption is > 99%.

2.4 Thermal modeling for 35 W and 100 W pump sources

To understand the thermal performance of our sapphire-Yb:YAG disk design shown in Fig. 3, we have build a finite-element model of the crystal assembly and simulated the behavior expected using both 35 W pump sources for Amplifier 1 and 100 W pump sources for Amplifier 2. The model was implemented using the code FlexPDE¹, and solved the fundamental CW heat equation

$$\nabla \bullet (k(T) \bullet \nabla T) + Q_h = 0, \quad (9)$$

where ∇ is the divergence and gradient operator expressed in Cartesian x , y , and z coordinates, k the thermal conductivity which is here a function of the temperature T , and Q_h is the heat power density of Eq. (6). Both the sapphire and Yb:YAG disks are treated in our model as isotropic. The edges and outer faces of the sapphire inside the indium annulus are assumed to be insulated as the entire crystal assembly is in vacuum. The disk diameter is 10 mm, and the indium annulus has a radial thickness of 2 mm, thus the clear face of the crystal assembly is 6 mm in diameter. The indium annuli, one on each sapphire face and in contact with an oxygen-free copper heatsink, were maintained at 77K in the model. We did not measure the actual crystal temperature achieved in the experiments described in this article, and thus cannot ascribe a thermal resistance to the two sapphire-indium annuli interfaces or to the copper crystal holder, however, based on our temperature measurements of

the crystal holder using a thermocouple, it is estimated that crystal temperatures at maximum pumping did not exceed 110-115 K. For those temperatures, ground-state absorption is still minimal in Yb:YAG.

2.4.1. FlexPDE, distributed by PDE Solutions Inc., Spokane Valley, WA 99206 USA

The modeling results to be shown here used the thermal conductivity fits shown previously in this paper for Yb:YAG with 10 at-% Yb doping and sapphire were entered into the model as continuously variable functions of temperature. The absorption function $A(z)$ of Eq. (5) was also used, and the pump source was assumed to be flat-topped with a diameter of 2 mm. For brevity, we will only present detailed 100 W pump source modeling results for amplifier 2 here.

2.5 100 W Pump source thermal results (Amplifier 2)

For the case of 100 W pump power per side incident upon the laser assembly, we show in Fig. 7. the heat power density in the center of the Yb:YAG crystal. The distribution is symmetric with respect to the center of the crystal, as expected for two-sided pumping, and reaches a maximum value of about 3.7 kW/cm³ at the faces in contact with the sapphire plates.

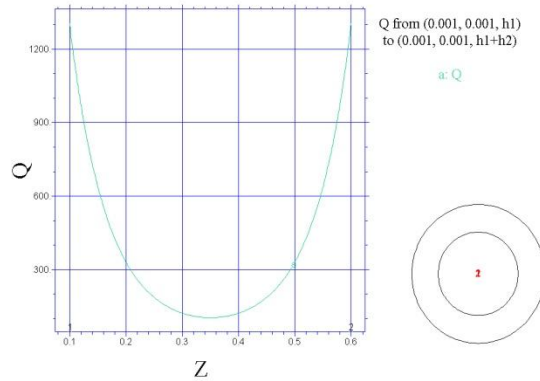


Fig. 7. Heat density Q as a function of Z coordinate deposited in the center of the Yb:YAG crystal.

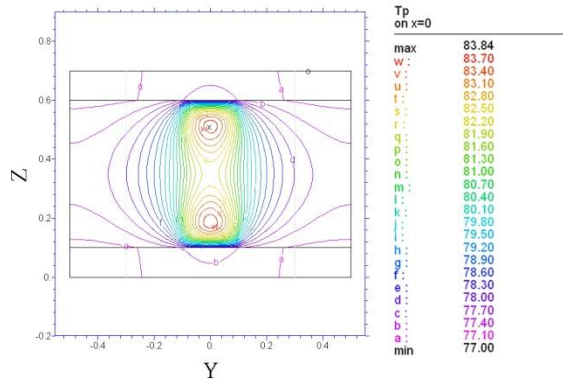


Fig. 8. Temperature distribution in the Z - Y plane through the center of the Yb:YAG crystal.

The temperature distribution in a Z - Y plane through the center of the crystal assembly is shown in Fig. 8. Z is the beam propagation direction and X and Y are the orthogonal

coordinates. The maximum temperature rise in the crystal is 21.4 K, and the temperature maxima occur inside the Yb:YAG crystal because of the rapid diffusion of heat near the crystal interface with sapphire having a much larger thermal conductivity. While there is transverse diffusion, almost the entire temperature rise is again contained in the ± 1 mm radial pumped region. The thermal gradients in the sapphire disks are minimal.

In Fig. 9, we show the heat flux vector field in the Z-Y plane through the center of the crystal assembly. This plot is a convenient way to visualize the transport of heat out of the Yb:YAG crystal and the transport through the sapphire to the indium annuli.

Figure 10 shows the radial temperature distribution at the outer face of the sapphire crystals, while Fig. 11 shows the radial temperature distribution in a plane located in the center of the crystal assembly. Figure 10 shows that at the sapphire interface the temperature rise is very small and well within the ± 1 mm pump region. The transverse distribution is not flat-topped because even near the faces of the Yb:YAG crystal some transverse diffusion occurs. Furthermore the distribution is parabolic like. In the center of the crystal, the temperature rise in the crystal on-axis is higher than at the sapphire interface, and transverse diffusion increases the width of the distribution in a logarithmic fashion beyond the ± 1 mm pump region.

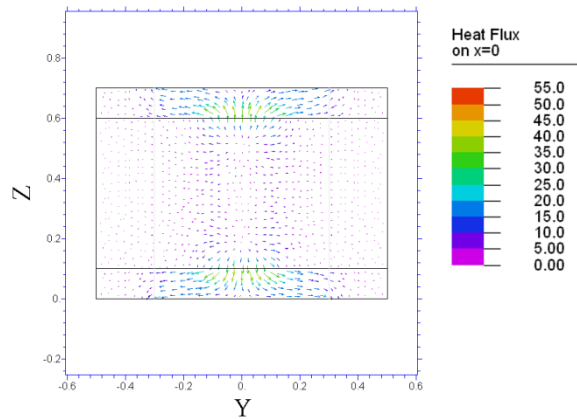


Fig. 9. Heat flux in the Z-Y plane through the center of the crystal assembly, showing the transport of heat out of the Yb:YAG disk, through the sapphire, and ultimately into the copper heat sink through the indium annuli.

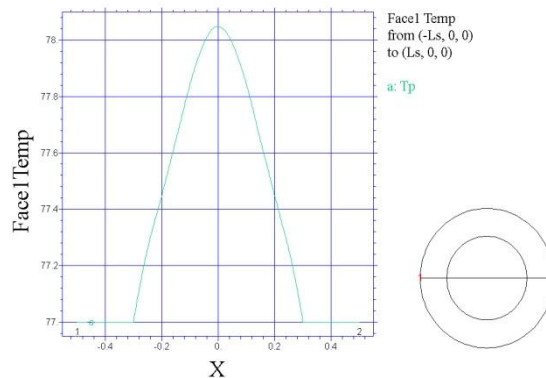


Fig. 10. Transverse radial temperature distribution at the outer faces of the sapphire crystals in contact with vacuum.

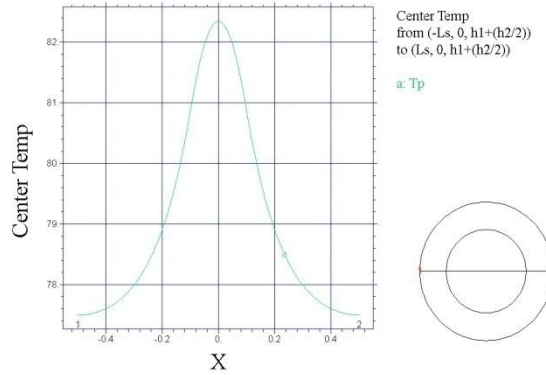


Fig. 11. Radial temperature distribution in the center of the Yb:YAG crystal.

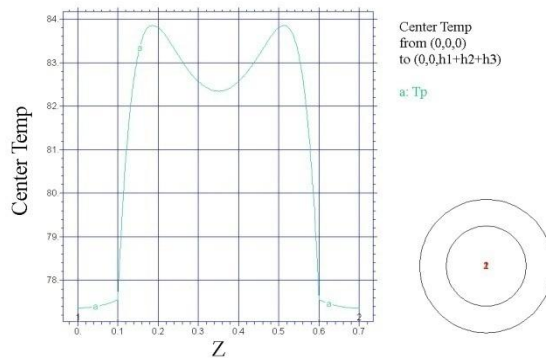


Fig. 12. Longitudinal temperature distribution through the center of the crystal assembly.

In Fig. 12, we show the longitudinal temperature distribution through the center of the crystal assembly. Two temperature maxima are located about 0.9 mm inside the Yb:YAG-sapphire interface with a value of about 98.4 K.

2.6 Phase distortion

We have calculated the expected phase distortion from disk assemblies for 35 W/side and 100 W/side pumping. In these calculations we have used the relationship

$$N(\mathbf{r}) = \frac{1}{\lambda_L} \int_0^{L_y} \beta \Delta T((\mathbf{r}, z)) dz, \quad (10)$$

where N is the number of waves, λ_L the laser wavelength, and β is the thermo-optic coefficient. ΔT is the temperature rise above 77 K in the crystal, a function of radius r and longitudinal coordinate z , L_y is the thickness of the Yb:YAG crystal (5 mm), and z the longitudinal coordinate. Because the phase distortion in the sapphire is insignificant, we have ignored it in the results presented here. Similarly, because the stress levels in cryogenically-cooled Yb:YAG crystals are so low, we have ignored any thermo-elastic contributions to the change in the index of refraction and have only calculated the results using the finite value of β discussed previously in this paper. Equation (10) was calculated using a finite-element program for nine radial values ($r = 0, 0.02, 0.04, 0.06, 0.08, 0.10, 0.12, 0.14, \text{ and } 0.16$ cm) and using longitudinal temperature values for each r generated by our FlexPDE program.

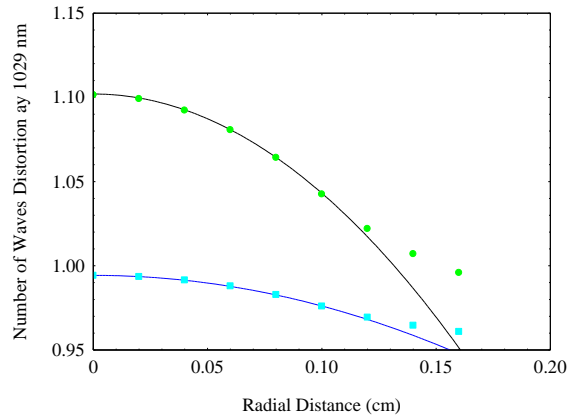


Fig. 13. Number of waves phase accumulation in Yb:YAG crystal as a function of radius for 35 W/side pumping (●), and 100 W/side pumping (◐).

The results are shown in Fig. 13. For the case of 35 W/side pumping (Amplifier 1), the phase difference between the center of the crystal at $r = 0$ and the $r = 0.16$ cm value amounts to about 0.033 wavelengths. For Amplifier # 1 with seven discrete Yb:YAG crystals, the total distortion through all seven disks amounts to 0.233 wavelengths. For 100 W/side pumping, the phase difference is calculated as 0.106 waves for a single crystal. For amplifier 2 with eight Yb:YAG crystals, the total phase accumulation is calculated as 0.845 waves. Ignoring phase distortion from any other elements in the laser system, the total phase distortion traversing Amplifiers 1 and 2 is 1.078 waves.

We also show in Fig. 13 quadratic fits to the phase data generated using the points at $r = 0$, 0.02, 0.04, 0.06, 0.08, and 0.10 cm. These fits show that inside the pump region extending to $r = \pm 1$ mm, the distortions are correctable, whereas for outside the pump region the distortions are largely uncorrectable.

The phase accumulation experienced by a beam traveling through the two cryogenic Yb:YAG amplifiers is very small, and is not expected to have a large effect on system beam-quality at the power levels reported in this paper. For the experiments reported here, the pump beam was approximately matched to the resonator mode with about a $1/e^2$ radius of 1 mm. The Gaussian extraction beam experiences mostly the correctable part of the phase distortion for $r \leq a$, where a is the pump beam semi-radius (1 mm), while the Gaussian region outside the pump region experiences a small un-correctable phase distortion out to the 99% encircled power radius at $r = 1.57$ mm.

2.7 Pump chamber design-distributed crystal assembly approach

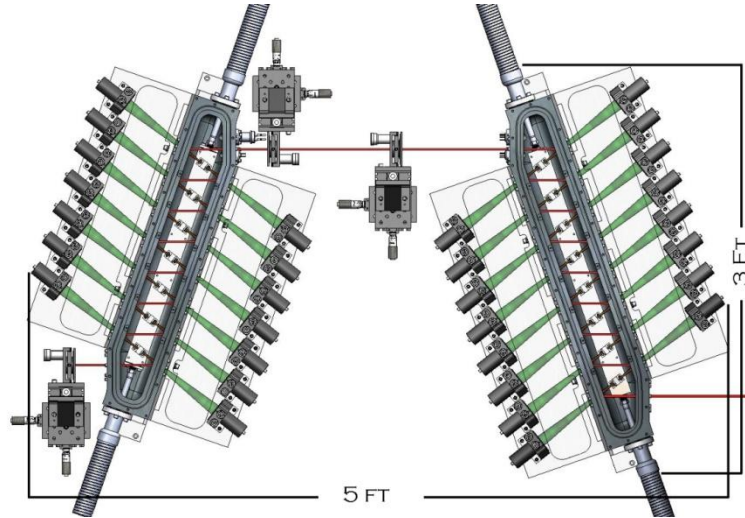


Fig. 14. Rendering of Yb:YAG Cryogenic CW Oscillator-Amplifier System.

Figure 14 shows a rendering of our CW cryogenic oscillator-amplifier system. Amplifier 1 on the left is used for the oscillator while amplifier 2 on the right is the power amplifier. Amplifiers 1 and 2 comprise aluminum pump chambers with forced cryogenic flow entering one end and exiting the opposite, a vacuum system to evacuate the pump chambers, eliminating condensation on optical surfaces, multiple 940 nm fiber-coupled pump sources that are imaged into each crystal, and imaging beam tubes to focus the diode light into the center of each disk. A cryogenic pump is used to provide flow rates up to 15 liters per minute through large oxygen-free copper heatsinks upon which the crystal assemblies are mounted. All laser diode pump sources are cooled and regulated using water based chiller systems whose temperature may be changed to match the diode center wavelength to the Yb:YAG absorption band near 940 nm. After traversal through AR coated fused silica windows to enter the interior of the pump chamber, the beam is zig-zagged back and forth to traverse the multiple crystal assemblies using low-loss dichroic mirrors that transmit the 940 nm pump light while reflecting the resonator or amplifier mode with a reflectivity that was originally $> 99.999\%$. The zig-zag path mimics that found in total-internal-reflection slab lasers, and results in a compact design. Amplifier 1 uses seven crystal assemblies identical to the one shown in Fig. 3, while Amplifier 2 uses eight. Each crystal assembly is pumped from opposite sides with 35 W/side for the oscillator and 100 W/side for the amplifier. A key feature of this laser is the use of distributed crystal assemblies rather than just a thick disk or rod; a major goal of this design was to minimize the maximum heating in any crystal assembly to less than 110 K, to minimize any thermal re-population of the laser terminal level. In that regard the design shown in Fig. 20 has been successful. The design is made possible by the use of high-quality dielectric coatings that minimize the single-pass loss. As will be discussed later in this article, however, we have found that the dichroic mirrors have suffered a significant performance degradation since their procurement, leading to a larger than expected linear loss. The cause of the degradation is not clear, and will be further investigated. The laser system shown in Fig. 14 is compact and has been found to be rugged, reliable, and capable of sustained operations for hours or days.

2.8 Stable long resonator

To form the oscillator resonator, we use 12.5 m long radius mirrors in a confocal arrangement to produce a large TEM_{00} spot diameter. The outcoupler has a reflectivity of 50% to maximize

the laser output and efficiency, and was optimized in previous experiments not discussed here. The HR mirror and the outcoupler produce an average beam $1/e^2$ diameter in the center of each Yb:YAG crystal of about 2.05 mm and spot diameters vary from 2.02 mm in the central crystal to 2.07 mm in the end crystals. The spot diameter on the HR and outcoupler is 2.1 mm. The total one-way resonator length is 171.84 cm.

The resonator discussed here has been found to be stable and to match the pump beam FWHM diameters of ~ 2 mm reasonably well. Our fiber-coupled diode sources typically produce higher-order super-Gaussian distributions that can be reasonably approximated as flat-top beams.

3. Laser data and analysis

3.1 CW laser performance

The CW Yb:YAG cryogenic laser system details are shown in Fig. 15. We present results here for an oscillator-amplifier system; the oscillator is formed using amplifier 1 and the resonator described in the aforementioned. Output from the oscillator is measured using a high power calorimeter at the output of the oscillator outcoupler. The output beam is then imaged using a 75 cm focal length lens into amplifier 2. The system can be operated as just an oscillator or as an oscillator-amplifier. Total system output was measured using a water-cooled calorimeter, and diagnostics including beam-quality, spectral, and temporal measurements were measured using the leakage from a high reflector at 1029 nm. A secondary low power stabilized calorimeter was also used to check the linearity of the primary power meter.

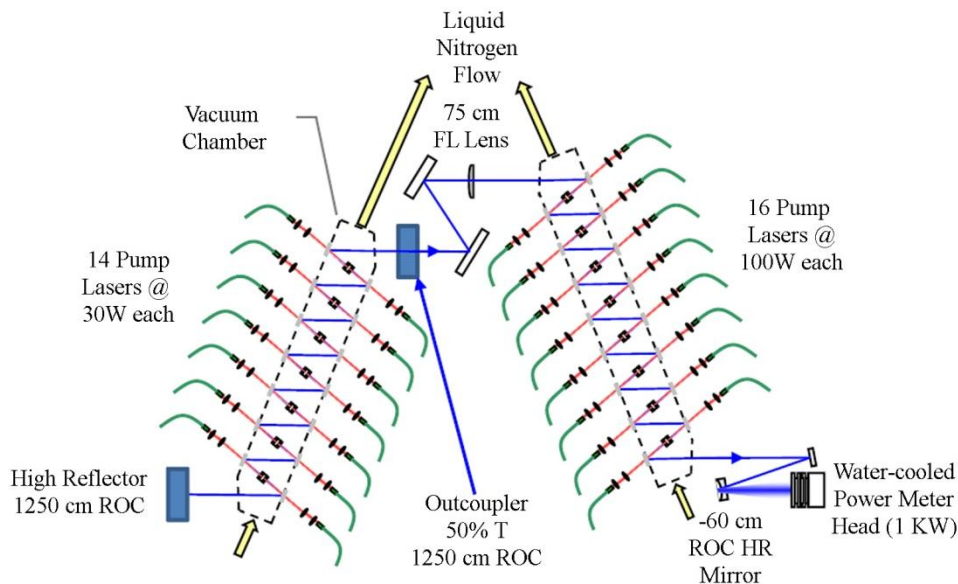


Fig. 15. CW Yb:YAG cryogenic laser system details.

Figure 16 shows the experimental CW data. The oscillator, which used an outcoupler with a measured reflectivity of 53.3% at 1029 nm, produced 211 W of output power and had a pump power threshold of about 48 W. The outcoupler value was optimized in previous experiments [12]. The output of the device was mostly linear with the exception of the final point at 501 W of input power, which rolled over slightly. This roll-over is due to insufficient capacity of the diode chiller to maintain temperature at maximum power, with the result that the wavelength of the diodes slew slightly towards the red and are less efficiently absorbed. This laser provides a high quality output beam that has a very symmetric beam profile with a TEM_{00} Gaussian spatial mode. The M^2 value was measured to be 1.2 ± 0.1 .

The CW output of the amplifier is also shown in Fig. 16. The output power for zero pumping of the amplifier is 163 W, and the maximum power measured for 1871 W of pump power was 963 W. The transmission of the amplifier for 211 W of power incident (zero pumping) is then 77%. The 23% loss was investigated in separate experiments. The transmission of the amplifier at 1029 nm with only the 16 dichroic mirrors in place was measured to be 94%, thus each dichroic mirror has a transmission of 99.61%, or a loss of 0.39%. This loss has changed since the installation of the mirrors when the loss was $< 0.01\%$. The source of the mirror degradation is not clear. Our vacuum system maintains a pressure of typically 10^{-3} torr, using an oil-free vacuum pump. It is possible that contamination of the mirrors occurred due to the use of impure cleaning solvents. The remainder of the single-pass transmission loss through the amplifier (13%) is alignment related, and occurs because of the edges of the amplified beam being slightly apertured passing through each crystal assembly and because there is a weak power-dependent wedging of the beam that results in a small vertical displacement as the power output is increased. Taking into account only the 6% passive transmission loss of the dichroic mirrors, this laser produced a calculated minimum of 1024 W at the highest pump power. In the future we will replace the dichroic mirrors and improve the passive transmission through the amplifier; those changes should produce a significant increase in the maximum average power reported here.

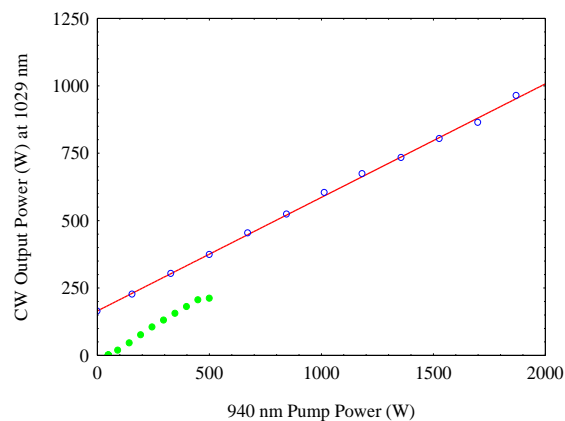


Fig. 16. Oscillator only (●) and oscillator-amplifier (○) CW output power at 1029 nm as a function of 940 nm pump power.

The beam-quality of the oscillator-amplifier system output has been measured at 600 W of average power out and the M^2 value found is 1.3 ± 0.1 .

The optical-optical efficiency of the amplifier was 44.4%, and the optical-optical efficiency of the entire oscillator-amplifier system was 42.2%, both quoted at maximum average power. These results can be improved by minimizing alignment losses in amplifiers 1 and 2, by better mode-matching (overlap efficiency) of the oscillator beam to the pumped volume in amplifier 2, and by increasing the ratio of the beam intensity/saturation intensity in both the oscillator and amplifier to achieve a larger extraction efficiency [25].

3.2 Ultrafast performance

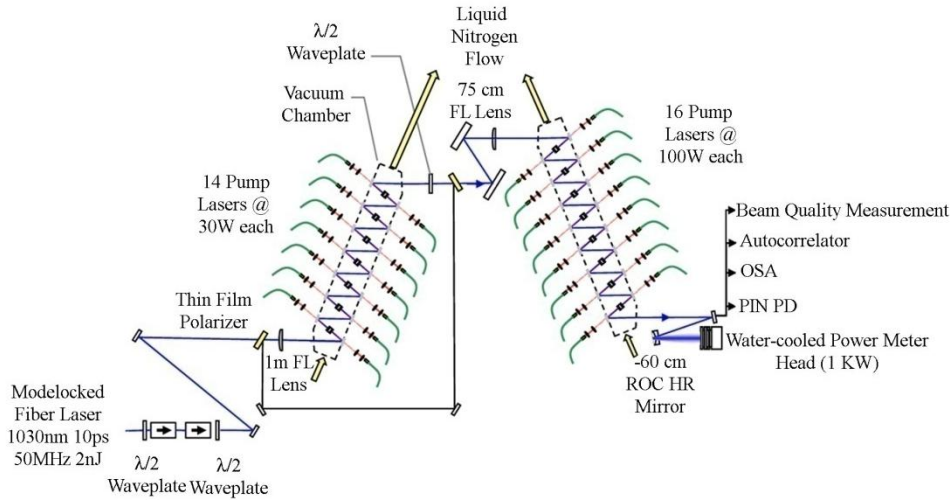


Fig. 17. Ultrafast Yb:YAG cryogenic laser system details.

Our ultrafast cryogenic laser system, shown in Fig. 17, uses the same amplifiers 1 and 2 discussed previously in this article. We used a direct picosecond amplification approach to avoid using a more complicated chirped-pulse-amplification (CPA) system; at the expected average power, approaching a kilowatt, and at a 50 MHz repetition rate, the peak pulse intensity expected was about 106 MW/cm^2 , well below the damage threshold for the optical component dielectric-coated surfaces in the amplifiers and the optical train. No optical damage was detected anywhere in the laser system. The system architecture we chose was to use a low average power Fianium mode-locked Yb fiber laser to drive a double-passed pre-amplifier as well as a single-passed power amplifier. Both amplifiers were pumped CW. The fiber laser had near-diffraction-limited output ($M^2 = 1.0 + 0.1, - 0.0$) and produced nominally 12 psec pulses with energy/pulse of about 1-1.5 nJ. The output beam from the fiber-laser was mode matched to the first pre-amplifier using a 1 m focal length AR coated lens. The fiber laser was isolated from the power amplification stages using two EOT Faraday rotators, with each providing 30 db of isolation. To increase the average power output from the first amplifier, the beam was double-passed using two thin-film polarizers and a half-wave plate. Leakage polarization pulses were eliminated by careful adjustment of the polarizers and the half-wave plate. After emerging from the thin-film polarizer at the output, the beam was imaged into the single-pass power amplifier using a 75 cm focal length AR coated lens. After exiting the power amplifier, the beam was incident upon a 1 kW water cooled power meter. As with the CW system discussed previously, various diagnostics were then employed to characterize the laser output, using the transmission leakage from a 1029 nm HR mirror. Measurement diagnostics included a fast photodiode and scope, an Ando optical spectrum analyzer, a beam-quality measurement system, a secondary calorimeter to check the linearity of the 1 kW power meter, and a Femtochrome autocorrelator to obtain pulsewidth measurements. The fiber laser produced an average power of up to 90 mW at a repetition rate of 50 MHz.

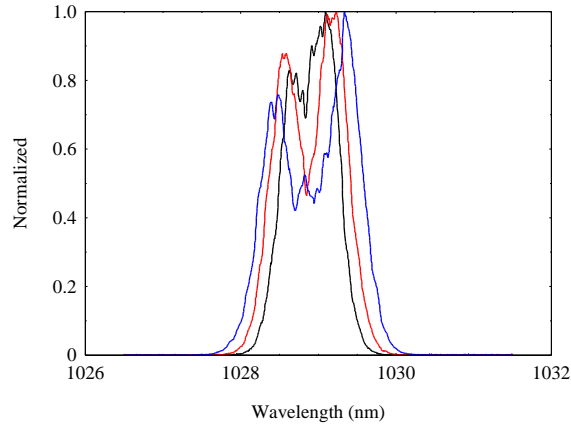


Fig. 18. Measured spectra of Fianium FM-1030-0.1-CST mode-locked fiber laser for 25 (—), 50 (—), 75 (—), and 90 mW (—) average power output. Superimposed on the output spectra is the Yb:YAG emission cross-section profile at 70 K.

In Fig. 18 we show output spectra of the Fianium fiber laser measured at 25, 50, 75, and 90 mW output average power. The FWHM spectral width increased from 0.48 nm at 25 mW to 1.325 nm at 90 mW. For the high average power experiments reported later in this paper, the fiber laser was operated near 50-55 mW output average power and thus the starting spectral width was about 0.815 nm. For average powers above 50 mW, the spectral output developed a pronounced dip in the center of the spectrum due to self-phase-modulation whose depth increased with average power. 50-55 mW of average power then represents a compromise between our desires to start with as much average power as possible and to minimize the modulation of the spectral output. The FWHM bandwidth of 0.815 nm is less than the 1.2 nm FWHM emission bandwidth of Yb:YAG at 70 K; Fig. 19 shows the emission cross-section of Yb:YAG as a function of wavelength and at temperatures of 70, 100, and 130 K [26]. It should also be noted that the peak emission cross-section wavelength is located at 1029.35 nm for 70 and 100 K, and slews to 1029.46 nm at 130 K. The peak emission from the fiber laser operating at 50-55 mW is located at 1029.1 nm, thus we expected that spectral redistribution would take place after propagating through amplifiers 1 and 2, and that the right hand side of the spectral distribution shown in Fig. 19 would be preferentially amplified with respect to the left hand side. This will be further discussed in the following.

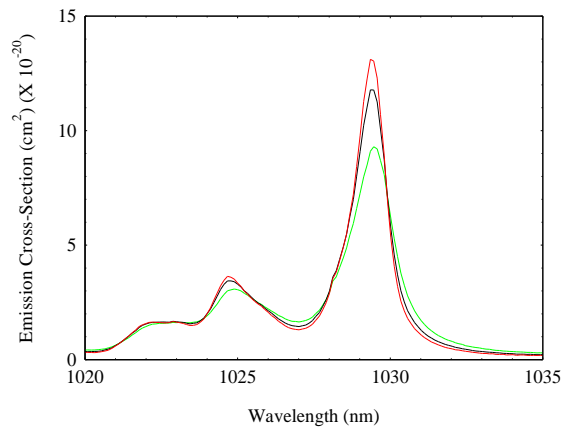


Fig. 19. Yb:YAG emission cross-section spectrum at 70 (—), 100 (—), and 130 K (—).

Figure 20 shows the average power output achieved with the system described here. After the pre-amplifier, an average power of 45.4 W is obtained for 55 mW of ultrafast input average power, or a power gain of 825. The maximum pump power was 341 W. After the single-pass power amplifier, as much as 758 W of average power was obtained, for a pump power of 1871 W. The roll-off evident in the data above about 1 kW of pump power is due to less than optimum mode matching and alignment, as well as a weak vertical beam displacement as average power increased. The gain in the second amplifier was about 17. The energy/pulse thus increased from 1.1 nJ at the oscillator output to 0.9 μ J after the double-passed amplifier, and finally to 15.2 μ J at the output of the single-passed power amplifier. Accounting for the linear loss in the power amplifier due to the dichroic mirrors, over 800 W of ultrafast power was actually produced. The optical-optical efficiency of the power amplifier was 39.6%, while the optical-optical efficiency of the entire ultrafast system was 35.6%.

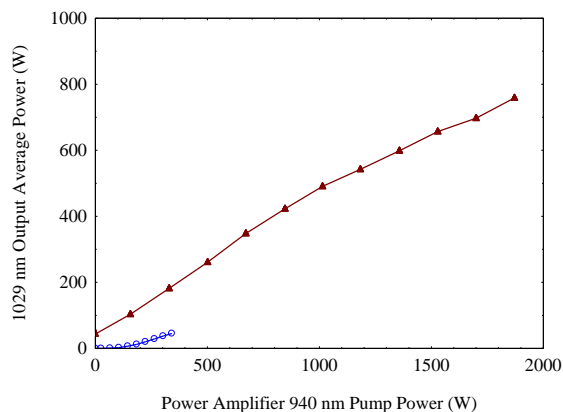


Fig. 20. Average power output of ultrafast Yb:YAG cryogenic laser system as a function of 940 nm pump power for amplifier 1 only (○) and amplifier 1 + amplifier 2 operation (▲), and for an average fiber laser input average power of 55 mW.

In Fig. 21, we show the measured output spectra after the double-passed amplifier. It can be seen that at 0.48 W out the spectrum has been redistributed and at 34 W out favors a single peak near 1029.6 nm. A spectrum taken after the single-passed power amplifier shown in Fig. 22, shows that at the higher average powers the main peak located near 1029.6 nm continues to grow while the secondary peak near 1029.4 nm becomes less intense. The spectral narrowing apparent from comparing Fig. 18, Fig. 21, and Fig. 22, is due to the preferential amplification of the fiber laser in the region near the Yb:YAG peak cross-section peak, or in the region around 1029.4-1029.5 nm.

Figure 23 shows the variation in the FWHM pulsewidth measured from the system output in the range of 0-500 W of average power using a Femtochrome Model FR-103HS autocorrelator, for assumed Gaussian or sech^2 pulse shapes. It is apparent that as average power increases, the FWHM pulsewidth does as well. The increase in pulsewidth is we believe correlated to the decrease in spectral bandwidth as average power increases, due to gain narrowing. While we were not able to measure pulsewidths above 500 W of average power in Fig. 23, we have used a second-order polynomial function to fit the data. Using the fitting functions for Gaussian and sech^2 pulses, we have estimated the pulsewidth at 750 W of average power out as 12.4 and 11.6 ps respectively. At the maximum average power output of 758 W, the energy/pulse was 15.2 μ J. If we assume a Gaussian pulse shape and a FWHM pulsewidth of 12.44 ps, the maximum peak power per pulse was 1.23 MW. The time-bandwidth product at 600 W of average power is estimated for a Gaussian profile using the calculated pulsewidth of 12.37 ps. From Fig. 22, the spectral width at 600 W is about 0.155 nm if only the large peak is used in the calculation. Using the pulsewidth of 12.37 ps,

we calculate a time-bandwidth product of 0.54, about a 23% deviation from the transform-limited value of 0.44. A similar calculation at 470 W of average power yields a time-bandwidth product of 0.65. We conclude that as the average power is increased and the spectrum of the system output tends towards a single peak, performance is trending towards transform-limited operation.

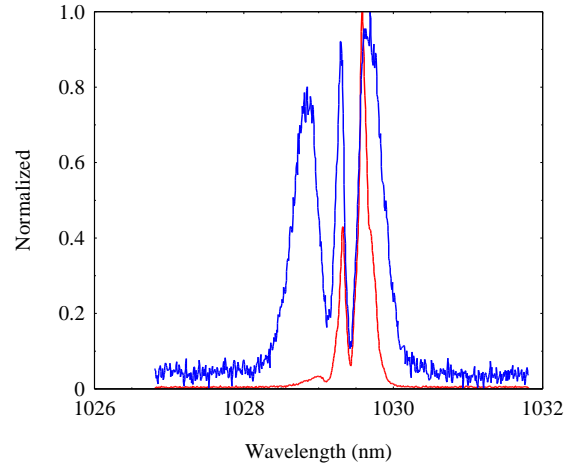


Fig. 21. Spectra at the output of the double-passed preamplifier, at 0.48 W output power (—) and 34 W output power (—).

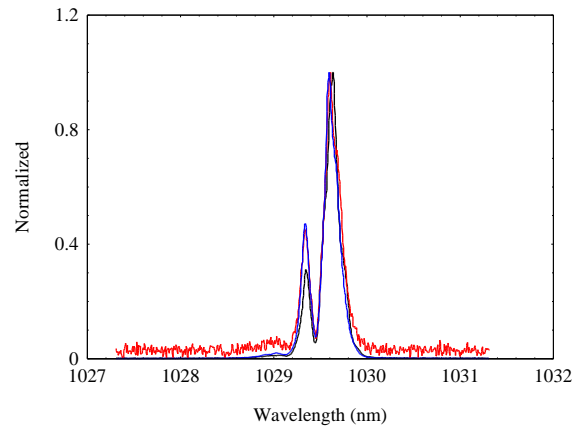


Fig. 22. Spectra at the output of the single-passed power amplifier for average powers of 341W(—), 470W(—), and 600W(—).

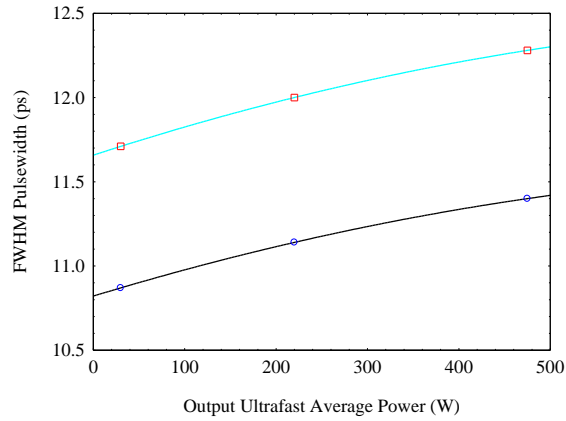


Fig. 23. FWHM pulsewidth as a function of ultrafast average power output for assumed Gaussian and sech^2 pulse shapes. The Gaussian pulse shape is denoted by \square and the sech^2 pulse shape by \circ . Data is derived from Femtochrome Model FR-103HS autocorrelator measurements.

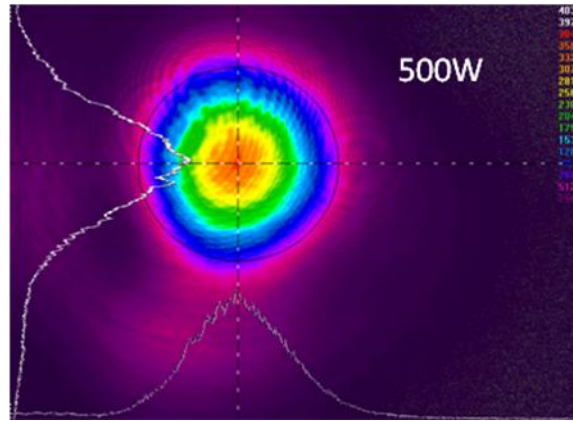


Fig. 24. Output beam profile at 500 W of ultrafast average power.

Figure 24 shows a spatial profile of the ultrafast system output at 500 W of average power. M^2 measurements performed at that power level yielded a value of 1.28 ± 0.1 . In Fig. 25, the 50 MHz pulse train exiting the single-pass power amplifier is shown at an average power out of 493 W. Pulse-pulse amplitude fluctuations of 4.83% were measured.

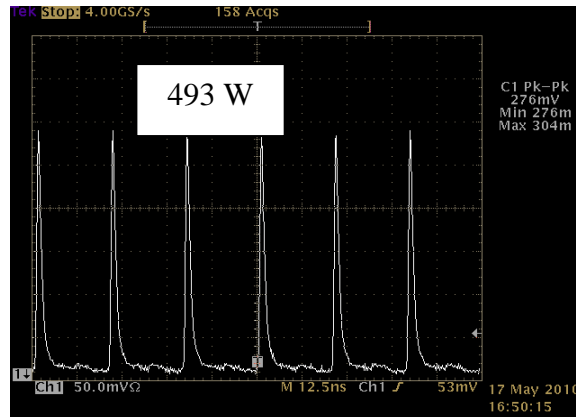


Fig. 25. Pulse train obtained at output of single-passed Yb:YAG power amplifier, at a repetition rate of 50 MHz and an average power of 493 W.

The high average power, short pulsewidths, and good beam-quality obtained with the system here indicate that this system is an excellent engine for the demonstration of high average power harmonic conversion. As an initial test of this assertion, we conducted a preliminary second harmonic generation experiment using a 20 mm long LBO crystal that was non-critically phase-matched in an oven maintained around 160 C and non-optimized optics. A negative beam expander was used to image the ultrafast beam into the LBO crystal, producing a $1/e^2$ diameter of about 2 mm. The results are shown in Fig. 26. For 160 W of input average power, about 60 W of 514.5 nm output power was obtained, or a conversion efficiency of 37.5%. At 160 W of average power the energy per pulse was 3.2 μ J, and the FWHM pulsewidth is estimated to be 11.8 ps, so the peak power was 271.2 kW. The peak intensity at the entrance to the LBO crystal was then about 17.3 MW/cm². A transverse beam profile of the green output beam is shown in Fig. 27. Polarization ratio was not measured at the output of amplifier 2, and we cannot with certainty state that the conversion efficiency was not degraded due to de-polarization of the fundamental beam, although the 37.5% conversion efficiency achieved with a peak input intensity of only 17.3 MW/cm² would seem to indicate a good polarization ratio. Future experiments will use higher input average and peak powers and are expected to yield much higher harmonic average power with conversion efficiencies greater than 70%.

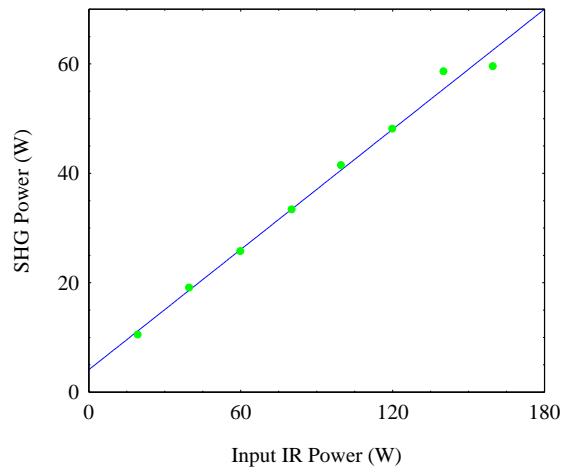


Fig. 26. Second harmonic (514.5 nm) output average power as a function of input infrared (1029 nm) average power from a NCPM LBO crystal.

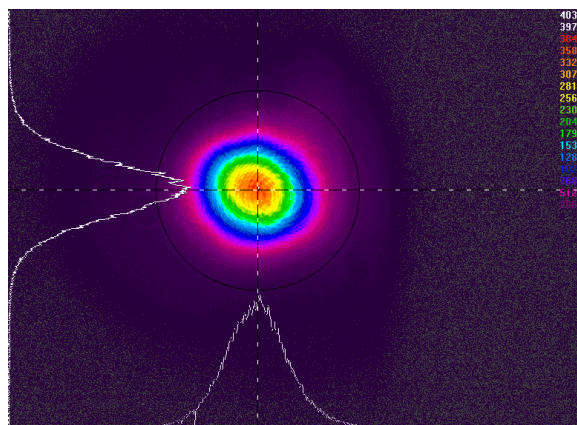


Fig. 27. Transverse beam profile of the second harmonic beam for 60 W of output power.

4. Discussion and conclusions

In this paper we have reported record performance for a cryogenic Yb:YAG laser operating in both CW and ultrafast configurations, and providing sustained power output for long periods of time. While both of the systems described need further development before optimal performance is obtained, the results to date show that cryogenic solid-state laser systems are capable of further scaling to much higher average powers, and that degradation of beam-quality that usually accompanies such scaling up may with proper design be largely avoided. The compact laser systems described here were realized by using a design that distributes the heat load over a number of crystal assemblies that were pumped with off-the-shelf commercially available 940 nm fiber-coupled diode sources, and were cooled using a custom liquid nitrogen forced-convection system. No crystal de-lamination or fracture problems have been encountered, and the system is capable of further orders of magnitude scaling while maintaining single-transverse-mode beam-quality, and without the use of wavefront correction methods. Furthermore, the output beam parameters remain nearly constant as laser output is varied, an important feature for many applications of interest including industrial machining applications and harmonic conversion. The high-average-power ultrafast laser described here is capable of producing record amounts of second, third, and fourth harmonic and optical parametric oscillator average power.

To summarize, we have demonstrated 963 W of CW output power and 758 W of ultrafast average power at 1029 nm. Both systems produced near-diffraction-limited output beams under sustained operating conditions. Preliminary second-harmonic-generation experiments have demonstrated the utility of the ultrafast configuration to produce high average power at 514.5 nm and higher harmonics. With further optimization, the system described here is capable of producing much greater than a kilowatt of average power in either operating mode. In the future, upgrades to the current system will substantially increase the optical-optical efficiency and average power output.

Acknowledgements

The authors are grateful to the U. S. Army Research Laboratory for support under Contract # W911NF-07-2-0048, and to Dr. S. Zhang of The Thomas Jefferson National Laboratory for providing the harmonic crystal and equipment used, and assistance in obtaining the second-harmonic generation results presented in this paper.